Research Article Vol. 33, No. 9 / 5 May 2025 / Optics Express 19257

Optics EXPRESS

Automated assembly of hybrid-integrated, chip-scale laser systems

TAYLOR LEVAUR,* XIAOLEI ZHAO, LANCE SWEATT, MOHAN GHIMIRE, AND LIN ZHU

Department of Electrical and Computer Engineering, Clemson University, Clemson, South Carolina 29634, USA
tlevaur@g.clemson.edu

Abstract: Hybrid photonic integration provides a platform to design and implement novel functionalities unavailable to active or passive material systems alone. We present an automated alignment and assembly process for hybrid-integrated laser systems, comprising silicon nitride (Si_3N_4) photonic integrated circuits (PICs) edge-coupled to gallium arsenide (GaAs) gain chips (GCs). We design and optimize spot size converters (SSCs) to increase the alignment tolerances between the PICs and GCs. Our automated assembly process has achieved experimental coupling losses of 2.7 dB between the PICs and GCs, closely matching the simulated values. Packaged hybrid lasers, when coupled to a lensed fiber, exhibit slope efficiencies of ~ 97 mW/A. These results show the feasibility of scaling the production and widespread application of these hybrid laser systems by automating their assembly, which should drive down packaging costs and accelerate research.

1. Introduction

Unlike the electronics industry, where CMOS is the predominant platform, photonic devices are integrated on a wide variety of material platforms because no material possesses the optimal properties for every application, or even most applications. For example, silicon has a small, indirect bandgap of 1.11 eV at 300 K that results in an absorption edge near 1 micron, which limits its usefulness in realizing low-loss waveguides (WGs) for visible photonics [1]. Stoichiometric silicon nitride (Si_3N_4), with its absorption edge at 400 nm, is more suitable for visible photonics, however, like silicon, it cannot provide an on-chip, electrically-pumped optical gain source without the incorporation of some direct bandgap III/V semiconductor materials. Thus, it is desirable to utilize the optimal material for each desired photonic functionality (such as Si_3N_4 for low-loss WGs and III-V for optical gain sources) and to realize optical systems by the hybrid integration of multiple passive and active chips.

Hybrid photonic integration is a proven approach driving many of the rapid advances in evermore demanding applications, such as quantum and atomic physics [2–5], free-space communications [6,7], sensing [8,9], LiDAR [9,10], optical processing [7,11], and AR/VR displays [12,13]. Some of these applications, which have high requirements for coherence and tunability, such as atomic physics, are supported by bulky and expensive bench-top tunable lasers, which provide the ultra-narrow linewidths and wavelength-tunability needed to access specific atomic transitions. Hybrid-integrated chip-scale laser systems [14–26] now match or even exceed the performance metrics of coherence, ultra-narrow linewidth, and wavelength tunability that is achievable by conventional bench-top tunable lasers, thus they show enormous promise for the miniaturization of these bulky instruments, which opens new opportunities for their application outside of well-controlled research environments.

A unique advantage of hybrid integration is that the design and processing of passive and active components may be independently optimized and tested before coupling, which also produces more reliable integrated devices. Furthermore, hybrid integration may rely on mature fabrication

#558968 https://doi.org/10.1364/OE.558968
Journal © 2025 Received 7 Feb 2025; revised 30 Mar 2025; accepted 10 Apr 2025; published 24 Apr 2025

processes without the need of incorporating unusual materials that complicate fabrication. In this report, we focus on hybrid integration based on active alignment. During active alignment of two or more photonic chips, their relative positions are optimized through the monitoring of an optical feedback signal. This process is typically done manually by mounting the chips on separate multi-axis mechanical stages. While this approach ensures precise alignment, it is not suitable for scalable manufacturing. By using a customized ficonTEC A300 active alignment machine, we demonstrate an automated process for the hybrid integration of passive PICs with active chips for various on-chip laser systems.

Our process relies on direct chip-to-chip edge coupling, the simplest form of hybrid integration, as it requires no intermediary media between the chips. While edge coupling features stringent requirements in alignment accuracy, it is robust across many different materials and applications. Unlike other coupling schemes, it does not require additional optical components or depend on refractive index contrasts. There are two critical factors for edge coupling: mode matching and cleaved facet quality. Tolerances for mode matching are expanded by use of SSCs to enlarge passive WG modes to better match the typically larger modes of III-V WGs or Single-Mode Fiber (SMF). To improve cleaved facet quality, we optimize the cleaving process for the passive PICs on silicon substrates. Cleaved facets of III-V chips usually have mirror-like surfaces, while achieving a high quality cleave for Si PICs is more challenging due to its hardness and the presence of several microns thick of amorphous silicon dioxide cladding layers.

Our automated process consists of three major steps. In the first step, the PIC is aligned a Fiber Array Unit (FAU) using an external tunable laser. Once this step is complete, each fiber of the FAU should be accurately aligned with a corresponding WG on the PIC. The next step is aligning the active chip to the PIC. In this work, we utilize a Fabry-Perot ridge waveguide laser diode (LD) as the active chip. The automatic alignment methodology investigated in this paper is entirely applicable to scenarios involving the utilization of a reflective semiconductor optical amplifier (RSOA) as the active chip. During this step, quasi-continuous wave (QCW) current is injected into the LD and the optical power collected by the FAU is used to optimize the alignment positions of the PIC and the LD. In the last step, the active chip and the passive PIC are initially separated, then an UV-curing epoxy is dispensed onto the PIC. A “wet” alignment is performed in the presence of epoxy since the optimal alignment positions may have slightly shifted during dispensing. Once an acceptable alignment is found, the epoxy is cured. This ensures that the alignment is not altered during the rest of the fabrication/testing process. This epoxy seal allows multiple devices to be rigidly mounted on a common submount for further packaging and testing. Our work develops an automatic alignment, assembly, and packaging process for hybrid lasers, which is crucial for realizing scalable manufacturing for practical applications. In addition, our approach enables multi-chip photonic integration, unlocking a wide range of potential applications.

2. Overview of A300 active alignment machine

Our ficonTEC A300 active alignment machine features a center vacuum-equipped chuck (CH1), a vacuum-based gantry pick-up-tool (PUT1), and left and right six-axis mechanical grippers (PUT2, PUT3 respectively), all placed atop a vibration-suppressing, self-leveling optical table. A labeled photograph of the A300 system is provided in Fig. 1, which also shows the orientation of the XYZ axes. The three translational axes are X (side-to-side), Y (back-and-forth), and Z (up-and-down). There are three rotational axes, one for each translational axis, that are named Rx, Ry, and Rz.

CH1 translates in Y and rotates in Rz. CH1 is used to mount the passive PIC, where the FAU and LD have sufficient clearance to align to the PIC without risk of collision. The vacuum of CH1 prevents movement of the PIC during the alignment process. CH1 provides a bottom-view IR camera that can also be converted to a side-view by means of a glass prism attached to a

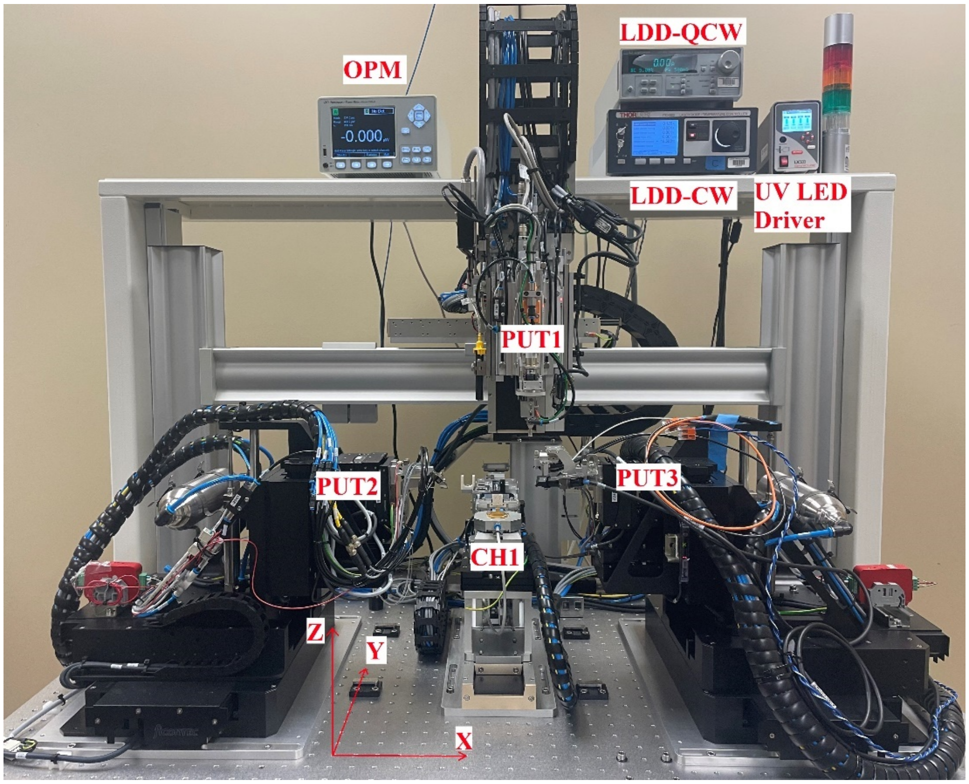

Fig. 1. Photograph of the customized A300 active alignment machine.

pneumatic slider. CH1 also features a vacuum-equipped FAU tray that eases the picking of the FAU by PUT2. Space for a standard sized Gel-Pak to be mounted for easy parts loading and unloading is also on CH1.

PUT1 translates in X and Z and rotates in Rz. PUT1 encloses a top-view IR camera that provides imaging to the machine vision system. There are two sliders attached to PUT1, one for an epoxy dispensing syringe and the other for the UV LEDs used during curing. The vacuum of PUT1 is used to gently handle the PIC. PUT2 is used for handling the FAU and features a slider with attached gripper that provides strain-relief to the collection of bare fibers exiting the glass block of the FAU. PUT3 is used for handling the LD and features a slider with attached pogo-pinned probes used to inject current into the LD.

A PC provides an interface between the necessary instrumentation, which consists of a tunable laser (Toptica DLC Pro), an optical power meter (OPM, Newport 2936-R), and a laser diode driver (LDD), and the motion control system of the A300. Figure 2 shows the electrical and optical connections between the PC, instrumentation, and the parts to be aligned. Ethernet allows the A300 to control the emission, wavelength, and injection current of the tunable laser. The BNC connection allows the A300 to record raw, analog power readings at the full 200 kHz sampling rate of the OPM. The RS232 connection allows the A300 to record calibrated, digital power readings at a 10 kHz measurement rate. The USB connection to the LDD allows the A300 to specify the injection current and switch the LD.

The light from the tunable laser is coupled into and out of the loopback WGs found on the left side of the PIC. The return signal is sent to a detector. A 3 dB splitter delivers half of the tunable laser output to each of the two loops. The MEMS switch allows the feedback from either loop to

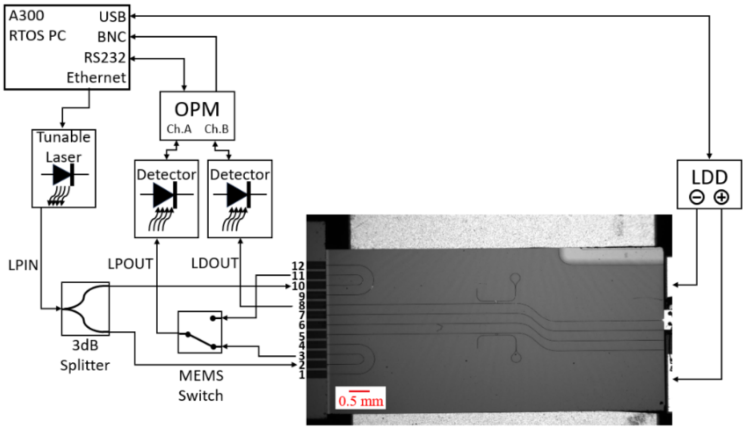

Fig. 2. Block diagram of A300 electrical and optical connections.

be switched to the detector used for the left-side alignment. Finally, a second detector is used to provide feedback for the right-side alignment. All fibers used in the system, except for the SMF spliced to the MEMS switch, are fast-axis-keyed polarization maintaining (PM) fiber using angle-polished connectors (APC).

3. Assembly process

The assembly process begins by loading the necessary materials into the A300. These materials consist of a Gel-Pak with the PIC and LD to be packaged, a fiber array unit (FAU) to couple laser light into and out of the PIC, and finally the epoxy needed for bonding. Left and right six-axis pick-up tools (PUTs) pick up the FAU and LD, respectively. Once the PIC is placed on CH1 by PUT1, the active alignment may begin.

Next, the "dry alignment" process begins by aligning the FAU to the PIC. A tunable laser (TL) is coupled from the FAU into one side of a loopback waveguide (WG). The WG-coupled beam exits the opposite side of the loop, and couples back into the FAU, which is then sent to a detector that quantifies the alignment accuracy. Usually, separate loopback WGs are present so that the FAU's rotation about the optical axis can be corrected. Once the FAU is aligned to the PIC, the FAU will collect light coupled into the PIC by the LD, and thus enables the LD to be aligned to the PIC. The alignment positions of the FAU, PIC, and LD are stored for later use in the "wet alignment".

The assembly process ends with the "wet alignment", which starts by moving the FAU and LD away to provide clearance for a syringe to dispense epoxy near the PIC-LD interface. After dispensing, the parts are returned to the previously stored alignment positions and a second active alignment is quickly performed as the epoxy dispensing process may have altered the optimal alignment position. Once the alignment is optimized in the presence of the epoxy, high-power UV LEDs are switched on to cure the epoxy. Finally, the packaged assembly is returned to the Gel-Pak using the gantry PUT. A more detailed description of the assembly process may be found in Supplement 1.

4. Design of passive PICs for automated assembly

Our passive PICs are fabricated on silicon substrates with a 4 μm thick bottom oxide (BOX), a 300 nm thick LPCVD Si_3N_4 device layer, and a 2 μm thick top oxide (TOX). This layer structure is used, along with a specified WG width, to simulate the power overlap between the fundamental mode of the PIC WG and the fundamental mode of the fibers found in the FAU at a wavelength of 970 nm. A flat-polished FAU is used in the assembly process, which has a nominal mode field diameter (MFD) of 6 µm and a fiber pitch of 250 µm. There is also the possibility of using a lensed FAU, which features a substantially smaller MFD than the flat-polished FAU. The FAU is AR coated to reduce reflections back into the external tunable laser and/or into the LD. Likewise, the LD and PIC facets could also be AR coated. However, our first designs implemented a self-injection locking configuration [24–26] on the PIC, which is less sensitive to reflection than the more common external cavity laser (ECL) [15–23]. In our case, some reflection was needed to form a laser cavity, thus we avoided coating our passive or active facets, which would have introduced additional complexity to process. If we wished to use an ECL configuration, we would likely need both AR coatings and angled waveguides to achieve the $R{\sim}10^{-4}$ reflectance required.

The bus WG width is set to 600 nm, which is narrow enough that only the fundamental TE and TM modes are supported. In the following discussion, we simulate the performance of both inverse tapers and regular tapers as SSCs to improve the mode matching between the PIC and LD/FAU. The inverse taper narrows the tip width from the width of the bus WG, whereas the regular taper widens the tip width from the width of the bus WG. Both inverse and regular tapers are useful for increasing the lateral mode size, however regular tapers are unable to effectively enlarge the vertical mode size.

Figure 3(a) shows the simulated coupling efficiencies of inverse (left) and regular tapers (right) coupled with the FAU fiber mode. Based on these results, the regular taper is roughly half as efficient as the inverse taper for coupling the FAU to the PIC, and thus it is ignored in later discussion. Although a FAU with 6 µm MFD is used in the assembly process, the tip width of the inverse taper is chosen to obtain the optimal overlap with the smaller 2-3 µm MFD of a lensed fiber. This is because we would later couple the assembled hybrid laser to the lensed fiber through this taper for further measurements once it fully packaged. Thus, we chose an inverse taper with a tip width of 150 nm, which provides a simulated peak coupling efficiency of 88.1% (-0.55 dB) when coupled to a 2.5 µm MFD fiber mode. This inverse taper provides a lower simulated coupling efficiency of 52.8% (-2.77 dB) when coupled to a 6 µm MFD fiber mode.

For the PIC to LD alignment, Figs. 3(b-c) display the simulated coupling efficiencies of inverse and regular tapers coupled to LDs of various ridge width and etch depths. The LD modes are simulated using an epitaxial layer stack defined by refractive indices and layer thicknesses. From Fig. 3(b), it can be observed that the regular and inverse tapers can both achieve similar coupling efficiencies with LDs of varying ridge widths. The maximum simulated coupling efficiencies provided by the regular taper (59.5% or -2.25 dB) are slightly higher than those provided by the inverse taper (52.7% or -2.78 dB).

The ridge etch depth is another parameter determining the LD mode size, and Fig. 3(c) shows the results of coupling the tapers to LDs of different ridge etch depths. With an increase in etch depth, the LD mode becomes more strongly confined, resulting in a reduction in the lateral MFD of the LD mode. Consequently, the optimal tip width for a regular taper becomes smaller, while the optimal tip width for the inverse taper becomes larger.

Then, we simulate the 1 dB alignment tolerance of various SSCs coupled to a LD with a ridge width of 7 µm and etch depth of 1100 nm, which is depicted in Fig. 4. As the tip width decreases, the inverse taper expands the mode size both laterally and vertically, resulting in a gradual expansion of its 1 dB alignment tolerance in both directions. In contrast, the regular taper can solely expand the mode size laterally, and consequently, increasing the tip width enhances the lateral tolerance, with no impact on the vertical tolerance. Note that, due to the epitaxial structure of our LDs, the LD mode exhibits an asymmetric profile in the vertical direction. As a result, the positive vertical tolerance curve differs from the negative vertical one. Based on the simulated results above, for the PIC and LD alignment, both inverse and regular tapers have their respective advantages. Therefore, we have incorporated both types of tapers in the PIC design. In order

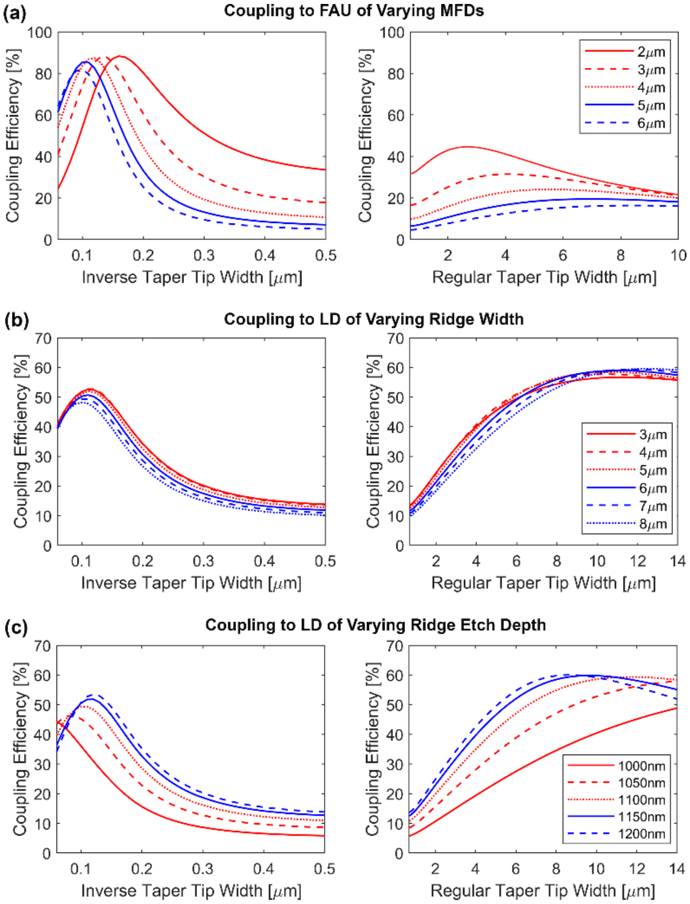

Fig. 3. Simulated coupling efficiencies of various SSCs coupled with (a) FAU of varying MFD, (b) LD of varying ridge width, (c) LD of varying ridge etch depth. In (b), the etch depth is set to be 1.1 μm, and in (c), the ridge width is set to be 7 μm.

to enable SSCs to accommodate LD modes of varying ridge dimensions, we finally chose the tip width to be 0.1 μm and 8 μm for the inverse and regular tapers, respectively. The 8 μm wide regular taper achieves a simulated coupling efficiency of 54.8% (-2.61 dB) accompanied by a 1 dB lateral tolerance of 1.66 μm and a 1 dB vertical tolerance of +0.25 μm/-0.21 μm. The 0.1 μm wide inverse taper achieves a simulated coupling efficiency of 49.2% (-3 dB) accompanied by a 1 dB lateral tolerance of 1.87 μm and a 1 dB vertical tolerance of +0.64 μm/-0.65 μm.

Another critical factor of edge coupling is the surface quality of cleaved facets. For our III-V active chips, it is easy to achieve high-quality facets via cleaving due to the crystalline atomic lattice of the III-V material (GaAs in the case of this work) and the material softness. Thus, the surface quality of the cleaved facets of our LDs are not the limiting factor in efficient coupling. The PIC facet quality, however, must be improved by optimizing the cleaving (scribe and break) process for the PICs on silicon substrates. This is accomplished by visual inspection of the chip facet using a microscope and assigning a numerical value of quality for straightness (no bends or deflections to the sides of the scribe line) and for smoothness (no hills or valleys). The primary parameters needing optimization are the scribe force, scribe angle, scribe length, impulse vs. anvil breaking, impulse bar pressure, and impulse bar dwell time. Shown in Fig. 5 are two

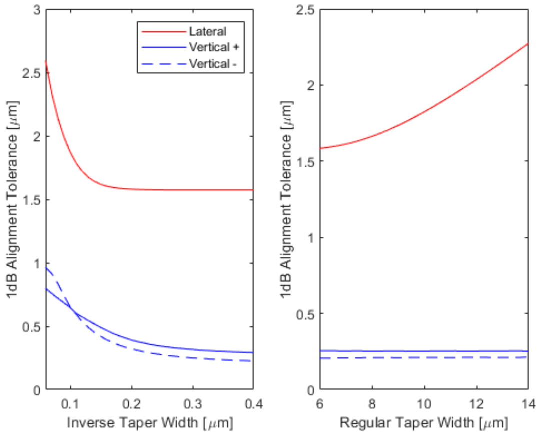

Fig. 4. Simulated 1 dB tolerances for the alignment of passive SSCs to a LD with ridge WG width of 7 μm and etch depth of 1100 nm.

examples of the cleaved facet of a passive PIC on a silicon substrate, one of high quality and the other of poor quality. As seen in the low quality cleave, the surface is not perfectly flat, which can hinder the proximity of the LD chip to the PIC, consequently severely limiting the coupling efficiency.

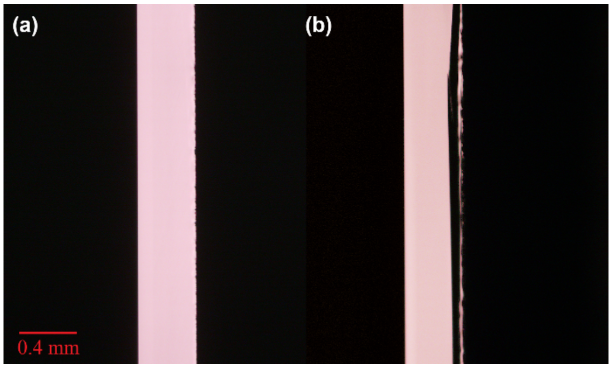

Fig. 5. Microscope images of the cleaved facet of a silicon substrate. Top substrate surface faces left in both images. (a) High quality cleave, (b) low quality cleave.

5. Results

Figure 6(a) displays the simulated (left) and measured (right) area scans for the dry alignment of a 150 nm wide inverse taper coupled to the flat-polished, 6 μm nominal MFD FAU used in the experiment. The 1 dB and 3 dB alignment tolerances are provided as contours on the respective area scans. The simulated and measured area scans are both circular Gaussian distribution, which is consistent with the mode profile of fiber mode. This indicates that the MFD of the inverse taper is smaller than that of the fiber mode, since it is known that the coupling maps between two modes is primarily determined by the mode profile of the larger mode. Our experimentally measured peak coupling efficiency falls within the range of -8 to -9 dB/facet depending on which loopback WG is used for alignment. The experimentally measured coupling efficiency is approximately 5-6 dB lower than the simulated value (-3 dB). To obtain a loss per facet measurement for the

PIC/FAU interface, we assume that the coupling at the one end of a WG loop will be the same at the other. We then measure the free space power of the benchtop tunable laser emission exiting the FAU, this is our reference power. After aligning the FAU to the PIC, we measure the power coupled from the PIC into the FAU and divide by the reference power. Thus, we obtain the total fiber-to-fiber loss, and can calculate the loss per facet by dividing the total loss by 2, which is why the earlier assumption is important. To obtain a loss per facet measurement for PIC/LD interface, we first measure the free space power of the LD, which gives the LD reference power. Next, we measure the total LD to PIC to FAU loss, and isolate the loss due to the PIC/LD coupling by subtracting out the loss per facet for the PIC/FAU interface from the total LD-to-PIC-to-PIC loss. The reported coupling loss is the average value of a number of experiments we performed. Note that the FAU to PIC coupling is not optimized since we mainly focus on minimizing the coupling loss between the PIC and LD in this work.

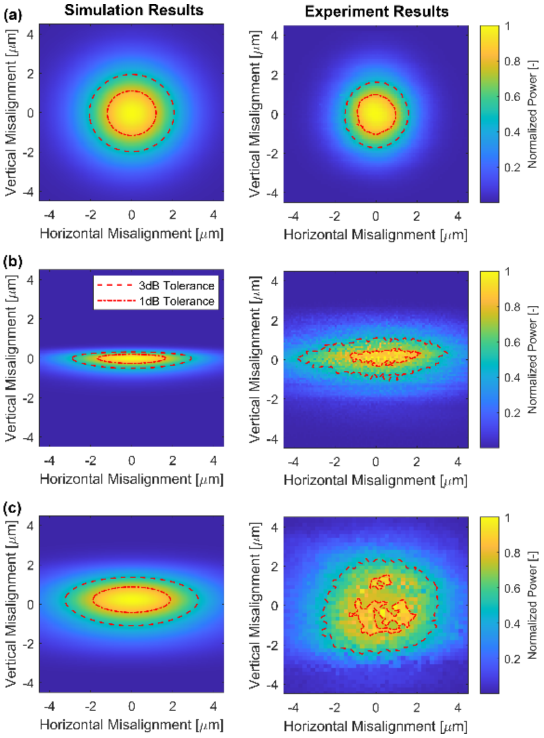

Fig. 6. Simulated and Measured Area Scans. (a) 150 nm width inverse taper SSC coupled to FAU, (b) 8 μm wide regular taper SSC coupled to LD, (c) 100 nm wide inverse taper SSC coupled to LD. A LD with ridge WG width of 7 μm and etch depth of 1100 nm was used for (b) and (c).

There are several factors that contribute to the reduction of coupling efficiency. First, the results reported above include the WG losses of the PIC. Second, due to the minimum gap spacing between the FAU and PIC, the 6 μm nominal MFD fiber mode will diverge a bit before arriving at the facet of the PIC, thus the actual FAU MFD may differ from what was used in simulation. Third, the inverse tapers coupled to the FAU are very narrow at 150 nm, which makes them highly susceptible to fabrication variations. Lastly, the FAU end-face and PIC facet may not have the best surface qualities, as both the FAU and PIC may be damaged by repeated touchdown procedures. Figure 7(a) shows the facet of a PIC used earlier in the process development when multiple touchdown procedures were performed during testing, whereas Fig. 7(b) shows the facet of a

PIC used after the process was developed and so only a single FAU touchdown was performed. Note that the BOX, Si_3N_4 device layer, and TOX are easily distinguishable for (b). Note that a well-developed process will likely only use one touchdown, or maybe two touchdowns depending on whether the stored dry alignment position yields an acceptable result at the beginning of the wet alignment, thus mitigating most of the risk of facet degradation.

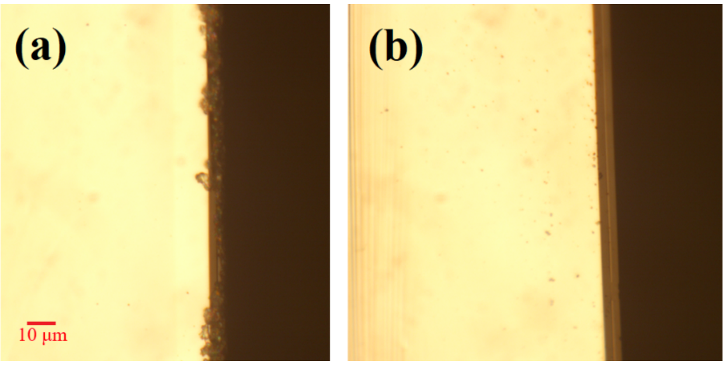

Fig. 7. Microscope images of cleaved facets of PICs on silicon substrates. (a) Multiple touchdowns performed, (b) single touchdown performed.

Figure 6(b) shows the area scan results for the alignment between the PIC and LD through an 8 µm wide regular taper. They exhibit a Gaussian profile in the lateral direction. However, in the vertical direction, it exhibits an asymmetric profile, which is attributed to the asymmetrical mode profile of the LD, as previously mentioned. We find that the coupling efficiency between the PIC and LD is significantly impacted by the distance between them. Note that this area scan exhibits more serious power fluctuations when compared with the area scan for the alignment between the PIC and FAU. This is because we utilize an uncoated FP LD as the active chips in our hybrid laser system. The optical feedback from the passive PIC to the LD introduces instability in the laser output of the hybrid system. Stable lasing output can be achieved through effective control of the feedback phase, as demonstrated in applications like on-chip self-injection locking or optical frequency comb lasers [24,25]. If the LD chip is replaced with a RSOA, the external cavity formed by the PIC and RSOA is expected to yield a more stable laser output.

Using a regular taper with a tip width of 8 µm, the highest coupling efficiency we have measured is about 2.65-3.65 dB/facet, depending on which loop is used to subtract out the PIC/FAU coupling loss. The measured coupling loss is very close to the simulated value (-2.6 dB), thus demonstrating that our automated assembly process can achieve efficient coupling between the PIC and LD. This result compares relatively well against previously reported results in literature for manual assembly/alignment processes of hybrid lasers. In 2019, Zhu et al. previously reported edge coupling of dual GaAs/InP RSOAs to a common Si_3N_4 PIC resulting in coupling losses less than 2 dB for their best samples, which utilized angled waveguides to reduce back reflections and improve coupling efficiency [16]. In 2022, Ghannam et al. reported simulated and measured coupling losses of 2.8 and 2.9 dB, respectively, for C and L band RSOAs edge coupled to Si_3N_4 PIC [27].

Figure 6(c) displays the area scan for the alignment of the PIC to the LD through a 100 nm wide inverse taper. As expected, the alignment tolerance in the vertical direction is much larger than that of the regular taper. However, we observe that the coupling efficiency using the inverse taper is much worse than using the regular taper, even though simulations indicate only a slightly lower coupling efficiency for the inverse taper compared to the regular one. It is believed that this is due to the fact that the narrow tip of the inverse taper is more susceptible to process variations than the regular taper. Thus, we only use the regular taper for the experimental demonstration of hybrid integrated lasers in this work.

Following the dry alignment, the wet alignment only requires a fine scan to recover the optimal alignment position and achieve a coupling efficiency close to that obtained during dry alignment. Upon completion of the epoxy curing, the hybrid integrated laser chip is finally obtained. Figure 8 depicts the top-view image of a completely bonded hybrid integrated laser chip.

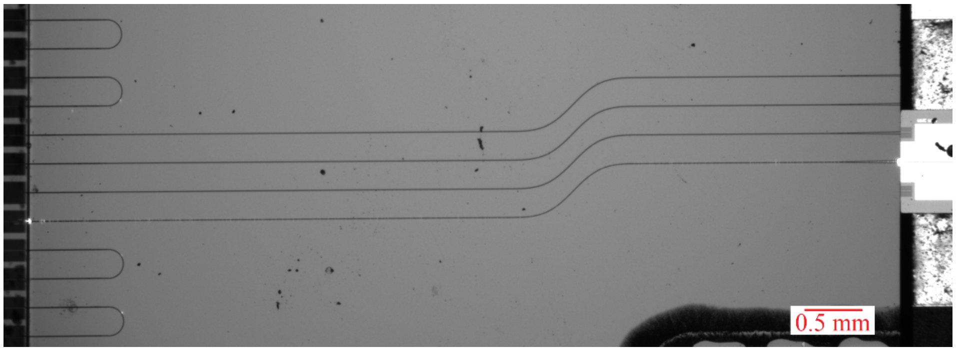

Fig. 8. Top-view camera image of completed wet alignment.

Optocast 3410 is used as the UV epoxy in our assembly process. A widely used epoxy with well-known bonding/curing characteristics was used to preempt the needed testing of many bonding/curing parameters. Only some preliminary testing was needed to configure the dispenser pressure and dispensing time such that a desired volume of epoxy was predictably dispensed at the desired location. Previously, when using a simple rectangular aluminum nitride LD submount with a width of 4 mm, we would observe a significant power loss of approximately 3-4 dB before and after epoxy curing [28]. We believe that power loss comes from the epoxy tending to spread over time and wandering across the entire chip facet during the alignment scans of the wet alignment. Using an updated T-shaped LD submount with a width of 8 mm, we were able to effectively eliminate this power loss by moving the epoxy sufficiently far away from the PIC/LD interface, thus preventing the epoxy from wicking into the air gap between the PIC and LD. Because the epoxy is dispensed sufficiently far away from the WG facet when using the T-shaped LD submount, there should be little difficulty expanding the operating wavelength band, as the device performance should be independent of the optical properties of the epoxy. One more point should be made about the epoxy; because even optical grade epoxies shrink during curing, it is important to implement mechanisms that compensate for the shrinkage (otherwise the alignment may shift during curing, thus resulting in worse coupling), such as ensuring uniform illumination of the epoxy by the UV LEDs and utilizing two dots of epoxy to counterbalance the shrinkages.

Once the newly bonded hybrid laser is successfully released by PUT3, the hybrid laser is mount atop a water-cooled copper stage for further performance characterization. Figure 9 illustrates a photograph of our measurement setup. In this setup, a vacuum is utilized to stabilize the hybrid laser position on the stage, two probes are employed for injecting current, and a lensed fiber with a nominal MFD of 2 μm is used to collect the laser output beam. It is worth noting that there exists a slight height difference between the bottoms of the PIC and LD submounts. This discrepancy primarily arises from the difference in chip thickness between the LD (approximately 125 μm) and the PIC (approximately 170 μm). Considering that the probe needles require a certain amount of pressure for good electrical contact with the LD submount, in our current setup, the LD submount is directly positioned on the stage, while the PIC submount overhangs the stage completely. In the near future, we plan to mount the hybrid laser onto a heat spreader using low temperature solder or thermally conductive epoxy to ensure better thermal dissipation for both the LD and PIC components. Not only will the common heatsink provide better thermal regulation for the hybrid laser, it should also significantly improve the robustness of our assembly. Currently, the hybrid laser is at least robust enough to allow the PIC to totally overhang the stage and still provide a good coupling from the LD into the PIC and from the PIC into the lensed fiber.

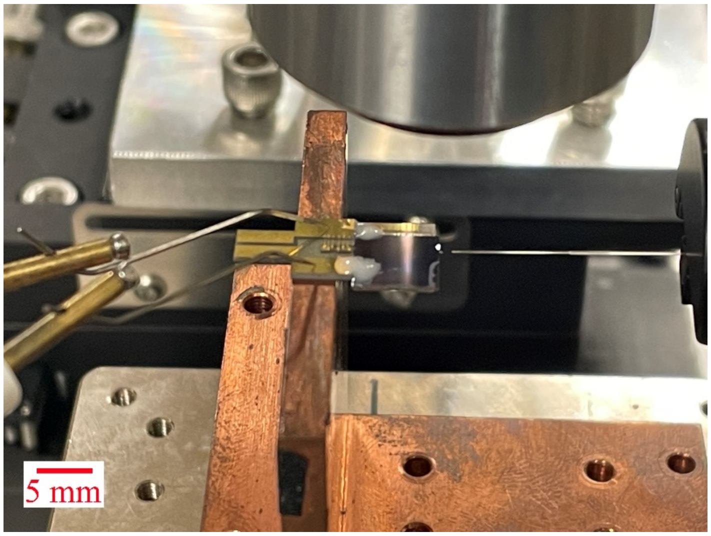

Fig. 9. Experimental setup for LIV curve measurement.

Figure 10 depicts microscope images captured by an IR camera mounted atop the microscope of the various features of the hybrid laser. The left image shows the LD that is permanently bonded to the PIC. The middle image shows the WG bends that help prevent the LD output from directly coupling to the fiber attached to the detector, which would confound the dry/wet alignment process. The right image shows the output facet of the hybrid laser, where the roughness of the facet scatters the light. Figure 11 illustrates the measured LIV curve of a well-packaged hybrid laser. From the LIV curve, we estimate the threshold current to about 65 mA and the slope efficiency of 97 mW/A when the laser output is coupled to a lensed fiber and about 178 mW/A when coupled to an integrating sphere. The integrating sphere is used to obtain an upper bound of the laser output power. The slope efficiencies reported above can be used to estimate the coupling loss of the PIC to the lensed fiber yielding an estimated coupling efficiency of 54.5% (-2.63 dB), which is comparable to 3 dB coupling loss we commonly see in our lab when coupling PICs to a lensed fiber. Furthermore, our reported slope efficiencies are based on the output power from one side of an uncoated diode laser, which compare well against established literature. In 2019, Zhu et al. reported slope efficiencies of 220 mW/A for the 1 μm emitting GaAs-Si_3N_4 hybrid laser, and 68 mW/A for the 1.55 μm emitting InP-Si_3N_4 hybrid laser. In 2024, Antman et al. reported edge coupling a 95 μm wide ridge waveguide Fabry-Perot laser to a Si_3N_4 PIC, resulting in a single mode output of 150 mW at a pump current of 3.2 A. Assuming a threshold of 300 mA from Fig. 2(b) in [29], their estimated slope efficiency is ~52 mW/A.

If we assume that the light collected by the integrating sphere only comes from the output facet of the PIC, the optical power measured by the integrating sphere is also a good estimate of the on-chip power. At an injection current of 175 mA, we estimate that the on-chip power is about 24 mW. It is important to note that this power can be doubled by applying a HR coating to the back facet of the LD, this is because the LD under test is uncoated.

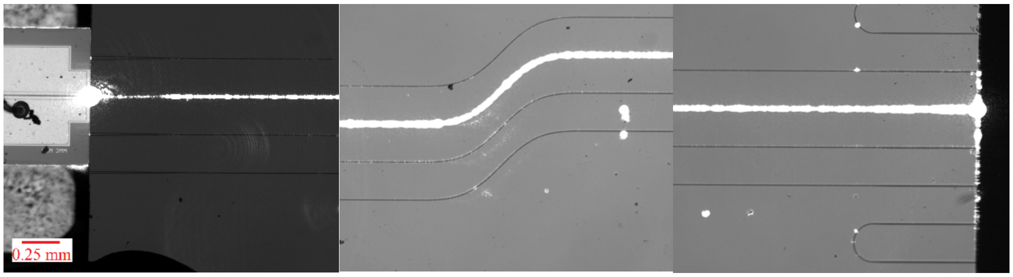

Fig. 10. Microscope images captured by IR camera. Left, LD/PIC interface, Middle, lossy WG bends, Right, hybrid laser output facet.

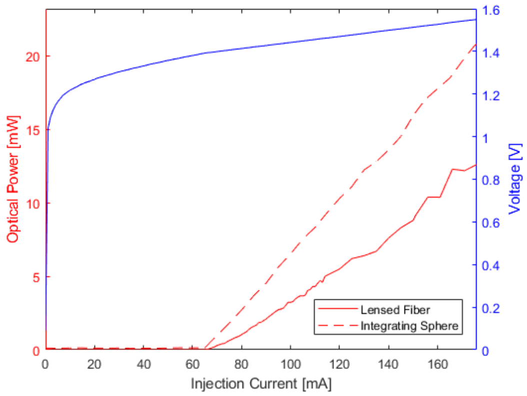

Fig. 11. Measured LIV curve of best hybrid laser to date.

6. Conclusion

We have presented an automated assembly process optimized for edge-coupled chip-scale hybrid laser systems with very efficient LD/PIC coupling. The design of various SSCs is investigated to increase the alignment tolerances and reduce the coupling loss. The packaged hybrid-integrated laser has a threshold current of about 65 mA and a slope efficiency of about 97 mW/A when coupled to lensed fiber. A maximum of 12.6 mW of fiber coupled power was detected at an injection current of 175 mA, yielding an estimated on-chip power of about 24 mW. Our devices demonstrate comparable performance to many reported results in terms of coupling efficiency and slope efficiency. In addition, our current test shows that the whole automatic alignment and assembly process is repeatable and has a very high yield, given both active and passive components are pre-tested. Another added benefit of our process is the possibility of multi-chip bonding/coupling. For example, multiple gain chips could be simultaneously coupled to a shared passive PIC. Current hybrid lasers mostly rely on manual alignment methods where each chip is separately mounted on independent translation stages. This limits how many chips can be simultaneously coupled together due to the size of the stages, however, by using our process, such restriction is greatly alleviated as we are not constrained by the size of stages, but by the size of our submounts/PIC. Our automated assembly process should enable the mass manufacturing of these hybrid lasers, thus reducing their cost and providing new markets for such technologies.

Funding. Army Research Office (W911NF-24-1-0034); National Science Foundation (2137776, 2329017).

Disclosures. The authors declare no conflicts of interest.

Data availability. Data underlying the results presented in this paper are not publicly available at this time but may be obtained from the authors upon reasonable request.

Supplemental document. See Supplement 1 for supporting content.

References

1. P. Kaur, A. Boes, G. Ren, *et al.*, "Hybrid and heterogeneous photonic integration," APL Photonics **6**(6), 061102 (2021).
2. R. J. Niffenegger, J. Stuart, C. Sorace-Agaskar, *et al.*, "Integrated multi-wavelength control of an ion qubit," Nature **586**(7830), 538–542 (2020).
3. N. Chauhan, J. Wang, D. Bose, *et al.*, "Ultra-low loss visible light waveguides for integrated atomic molecular and quantum photonics," Opt. Express **30**(5), 6960 (2022).
4. A. Isichenko, N. Chauhan, D. Bose, *et al.*, "Photonic integrated beam delivery for a rubidium 3D magneto-optical trap," Nat. Commun. **14**(1), 3080 (2023).
5. C. W. Hogle, D. Dominguez, M. Dong, *et al.*, "High-fidelity trapped-ion qubit operations with scalable photonic modulators," npj Quantum Inf **9**(1), 74 (2023).
6. J. Bütow, J. S. Eismann, V. Sharma, *et al.*, "Generating free-space structured light with programmable integrated photonics," Nat. Photonics **18**(3), 243–249 (2024).
7. M. Milanizadeh, S. SeyedinNavadeh, F. Zanetto, *et al.*, "Separating arbitrary free-space beams with an integrated photonic processor," Light. Sci. Appl. **11**(1), 197 (2022).
8. J. Milvich, D. Kohler, W. Freude, *et al.*, "Integrated phase-sensitive photonic sensors: a system design tutorial," Adv. Opt. Photonics **13**(3), 584 (2021).
9. L. Tang, L. Li, J. Li, *et al.*, "Hybrid integrated ultralow-linewidth and fast-chirped laser for FMCW LiDAR," Opt. Express **30**(17), 30420 (2022).
10. A. Lukashchuk, H. K. Yildirim, A. Bancora, *et al.*, "Photonic-electronic integrated circuit-based LiDAR engine," Nat. Commun. **15**(1), 3134 (2024).
11. W. Bogaerts, D. Pérez, J. Capmany, *et al.*, "Programmable photonic circuits," Nature **586**(7828), 207–216 (2020).
12. R. N. Frentrop, D. H. Geuzebroek, E. J. Klein, *et al.*, "Hybrid integrated RGB light engine for AR in silicon nitride PIC technology," *Proc. SPIE (AR VR MR IV)*, 12449(124490F), (2023).
13. D. Geuzebroek, R. Frentrop, R. Dekker, *et al.*, "Small and scalable laser source for AR glasses by hybrid integration of silicon nitride PIC technology," *Proc. SPIE (AR VR MR V)*, 12913(129130R), (2024).
14. M. Li, L. Chang, L. Wu, *et al.*, "Integrated Pockels laser," Nat. Commun. **13**(1), 5344 (2022).
15. H. Guan, A. Novack, T. Galfsky, *et al.*, "Widely-tunable, narrow-linewidth III-V/silicon hybrid external-cavity laser for coherent communications," Opt. Express **26**(7), 7920 (2018).
16. Y. Zhu and L. Zhu, "Narrow-linewidth, tunable external cavity dual-band diode lasers through InP/GaAs-Si3N4 hybrid integration," Opt. Express **27**(3), 2354 (2019).
17. Y. Fan, A. van Rees, P. J. M. van der Slot, *et al.*, "Hybrid integrated InP-Si3N4 diode laser with a 40-Hz intrinsic linewidth," Opt. Express **28**(15), 21713 (2020).
18. W. Jin, Q. Yang, L. Chang, *et al.*, "Hertz-linewidth semiconductor lasers using CMOS-ready ultra-high-Q microresonators," Nat. Photonics **15**(5), 346–353 (2021).
19. E. Shim, A. Gil-Molina, O. Westreich, *et al.*, "Tunable single-mode chip-scale mid-infrared laser," Commun. Phys. **4**(1), 268 (2021).
20. H. Nejadriahi, E. Kittlaus, D. Bose, *et al.*, "Sub-100 Hz intrinsic linewidth 852 nm silicon nitride external cavity laser," Opt. Lett. **49**(24), 7254 (2024).
21. J. Xie, L. Lou, X. Yan, *et al.*, "Hybrid-Integrated Dual III-V/Si3N4 Laser Module for Widely Tunable Terahertz Generation," J. Lightwave Technol. **42**(24), 8859–8868 (2024).
22. A. D. White, G. H. Ahn, R. Luhtaru, *et al.*, "Unified laser stabilization and isolation of a silicon chip," Nat. Photonics **18**(12), 1305–1311 (2024).
23. J. Wang, X. Li, X. Guo, *et al.*, "Scalable single-microring hybrid III-V/Si lasers for emerging narrow-linewidth applications," Opt. Express **32**(15), 26751 (2024).
24. J. Ling, J. Staffa, and H. Wang, "Self-Injection Locked Frequency Conversion Laser," Laser Photonics Rev. **17**(5), 2200663 (2023).
25. M. Corato-Zanarella, A. Gil-Molina, X. Ji, *et al.*, "Widely tunable and narrow-linewidth chip-scale lasers from near-ultraviolet to near-infrared wavelengths," Nat. Photonics **17**(2), 157–164 (2023).
26. A. S. Voloshin, N. M. Kondratiev, G. V. Lihachev, *et al.*, "Dynamics of soliton self-injection locking in optical microresonators," Nat. Commun. **12**(1), 235 (2021).
27. I. Ghannam, B. Shen, F. Merget, *et al.*, "Silicon Nitride External Cavity Laser with Alignment Tolerant Multi-Mode RSOA-to-PIC Interface," IEEE J. Sel. Top. Quantum Electron. **28**(1: Semiconductor Lasers), 1–10 (2022).
28. X. Zhao, T. LeVaur, L. Sweatt, *et al.*, "Hybrid Integrated Chip-Scale Laser Systems Based on Automated Assembly," *74th Electronic Components and Technology Conference* (IEEE, 2024), pp. 1179–1186.
29. Y. Antman, A. Gil-Molina, O. Westreich, *et al.*, "High power chip-scale laser," Opt. Express **32**(26), 47306 (2024).